Spectrochimica Acta Part A: Molecular and Biomolecular Spectroscopy 260 (2021) 119869

Contents lists available at ScienceDirect

Spectrochimica Acta Part A: Molecular and Biomolecular Spectroscopy

journal homepage: www.elsevier.com/locate/saa

The influence of intermolecular correlations on the infrared spectrum of liquid dimethyl sulfoxide

Maciej Śmiechowski *

Department of Physical Chemistry, Faculty of Chemistry, Gdańsk University of Technology, Narutowicza 11/12, 80-233 Gdańsk, Poland

HIGHLIGHTS

- Ab initio molecular dynamics reveals the structure and dynamics of liquid DMSO.
- Decomposed infrared spectra show considerable contribution of the intermolecular term.
- Two-dimensional correlation spectra reveal trends in distance-dependent IR response.
- Three-dimensional decomposed IR response shows complex spectral patterns.

GRAPHICAL ABSTRACT

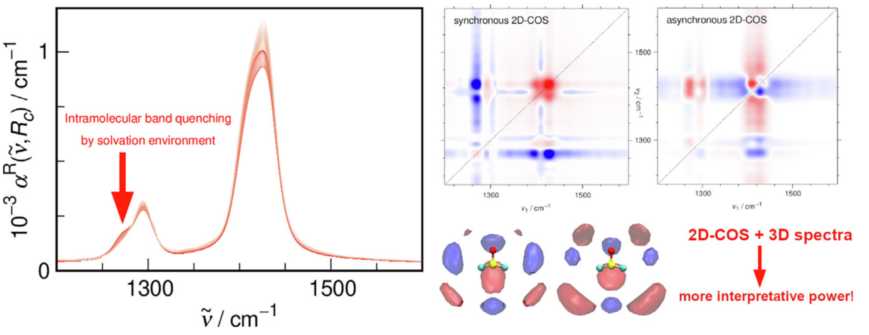

ARTICLE INFO

Article history:
Received 2 February 2021
Received in revised form 9 April 2021
Accepted 21 April 2021
Available online 27 April 2021

Keywords:
Dimethyl sulfoxide
Ab initio molecular dynamics
Infrared spectroscopy
Spatially resolved infrared spectra
Generalized two-dimensional correlation spectroscopy

ABSTRACT

Dimethyl sulfoxide (DMSO) is routinely applied as an excellent, water-miscible solvent and chemical reagent. Some of the most important data concerning its liquid structure were obtained using infrared (IR) spectroscopy. However, the actual extent of intermolecular correlations that connect the isolated monomer spectrum to the IR response of the bulk liquid is poorly studied thus far. Using ab initio molecular dynamics (AIMD) simulations, IR spectra of liquid DMSO are obtained here from first principles and further analyzed using an array of sophisticated spectral decomposition techniques. The calculated spectra when unfolded in space reveal non-trivial spatial correlations underlying the IR response of liquid DMSO. It is unequivocally demonstrated that some of the fundamental vibrations visible in the intramolecular limit are effectively suppressed by the solvation environment due to symmetry reasons and thus disappear in the bulk limit, escaping experimental detection. Overall, DMSO as an aprotic solvent with dominant dipole–dipole interactions displays strong intermolecular correlations that contribute significantly to the IR spectra, on par with the situation observed in strongly associated liquids, such as water.

Introduction

Dimethyl sulfoxide (DMSO) is very widely used as an excellent, water-miscible solvent [1–3] and chemical reagent [4]. It is also applied as an important cosolvent in solvent mixtures with tunable properties [5]. In life sciences, it serves as a universal drug carrier in medicinal chemistry [6] and a radio- and cryoprotective agent in cell biology [7].

DMSO is often regarded as a prototypical dipolar aprotic solvent [1]. It is characterized by a considerable dipole moment (3.96 D in the gas phase [8]) and a large static permittivity (47 [9]). Its applicability as a solvent is further expressed by moderate viscosity (1.985 mPa s [10]) and a broad liquid range (18.5–190 °C [11,12]). Accordingly, it is completely miscible with both water

---

* Corresponding author.
E-mail address: maciej.smiechowski@pg.edu.pl

https://doi.org/10.1016/j.saa.2021.119869
1386-1425/

and numerous organic solvents [5] and many inorganic salts show decent solubility in DMSO as well [13].

The structure of liquid DMSO was studied directly with X-ray and neutron diffraction methods [14–17]. Hence, both the intramolecular structure of the liquid, as well as the intermolecular distances are experimentally well researched. The structure and dynamics of liquid DMSO was also the subject of numerous computational studies, namely quantum chemical calculations [18–20,15], molecular dynamics (MD) simulations [18,21–23,15,24–30,16] and Monte Carlo (MC) studies [31,14].

Vibrational spectroscopy is a well established method for studying the intermolecular interactions in molecular liquids [32]. Accordingly, it was often applied for elucidating the nature of intermolecular couplings in liquid DMSO. The detailed assignment of fundamental vibrations of DMSO has been available for some time [33–35]. To date, both infrared (IR) [18,36,37,33,38,39,34,35] and Raman spectroscopy [19,40–42,33,43,44] were used to unravel the intermolecular interactions in liquid DMSO either in the entire IR range or for selected fundamental bands only. Several of those previous investigations concerned the estimation of the degree of molecular association (primarily dimerization) in liquid DMSO [18,38–41,43]. While vibrational spectra were often interpreted in terms of discrete component bands stemming from well defined associates, the results of other methods, primarily dielectric relaxation, are inconclusive and hint at a lack of strong orientational correlations in liquid DMSO [45–50].

In the search for a molecular level description of the dipolar couplings that ultimately underlie the intermolecular part of the IR spectrum, computational spectroscopy based on rigorous partitioning of the system's dipole moment into discrete fragments offers an unsurpassed explanatory power [51–54]. The more advanced smooth decomposition schemes for dipole moments currently available were instrumental in deciphering the spatial correlations modulating the IR spectrum of liquid water [51,52]. We have recently demonstrated that this formalism is fully transferable to anisotropic molecular liquids [55,56]. The simulation tool of choice in such investigations is definitively ab initio molecular dynamics (AIMD) that combines quantum mechanical representation of the electron density with the nuclei trajectories determined according to the classical laws of motion [57]. Although AIMD has been the state of the art in liquid water simulations for the last two decades [58], the increased demand on computational resources dramatically limited its applicability in the studies of larger molecular solvents. Nevertheless, the investigations of polar aprotic solvents and other complicated liquid systems with AIMD simulations are currently an emerging area of computational studies [55,56,59–62].

Recently, we demonstrated the usefulness of computational spectroscopy for the purpose of decomposition of IR spectra into well-defined intermolecular contributions on the example of liquid γ-butyrolactone (GBL) [55,56]. Herein, we report on a follow-up study aimed at deciphering the cross-correlations in the IR spectra of liquid DMSO. Although its aqueous mixtures were the subject of AIMD investigations in the past [63,36,64,65], the neat liquid was studied only once in a system of a very limited size [36]. This work undertakes a comprehensive analysis of the measurable IR spectrum of liquid DMSO at ambient conditions in terms of the distance-dependent and spatially resolved IR spectra that provide a molecular level explanation for the spectral modulations from the monomolecular approximation up to the bulk limit. Additionally, we propose a novel application of the generalized two-dimensional (2D) correlation spectroscopy (2D-COS) [66] that enables a more meaningful comparison of the distance-dependent IR response at different spectral regimes and allows for a classification of the fundamental bands into discrete sets differing with respect to the IR response modulation. Once again, it is conclusively demonstrated that moderately associated molecular liquids with short-range structure dominated by dipole–dipole interactions display complicated IR spectral patterns when seen from the spatially resolved perspective.

Spectral analysis methodology

In the framework of linear response theory, the linear absorption coefficient of a system is calculated as a Fourier transform (FT) of the total dipole moment time correlation function (TCF) [67–69],

$$\alpha(\omega) = \mathscr{F}(\omega)\int_{-\infty}^{\infty} \mathrm{d}t\, e^{-i\omega t}\langle \boldsymbol{M}(t_0+t)\boldsymbol{M}(t_0)\rangle, \tag{1}$$

where $\langle\ldots\rangle$ denotes an ensemble average and $\mathscr{F}(\omega)$ is the quantum correction prefactor to the classical total dipole moment TCF [68]. It is often preferable to work with the origin-independent total dipole moment derivative, $\dot{\boldsymbol{M}}$, however, since true dipole velocities are usually not available, it must be approximated in practice by taking finite differences, $\dot{\boldsymbol{M}} \approx \delta\boldsymbol{M}/\delta t$, where δt is the time step of the dipole moment trajectory.

We would like to formally decompose the total dipole moment from Eq. (1) into discrete molecular dipole moments, i.e., $\boldsymbol{M} = \sum_{i=1}^{N}\boldsymbol{\mu_i}$. Using the maximally localized Wannier functions (MLWFs) formalism [70], such an unambiguous partitioning in the condensed phase is made possible [71]. The desired molecular dipole moments are then obtained classically by summing over positive nuclei and negative MLWF centers within a molecule. We note in passing that alternatives to the computationally expensive orbital localization exist, such as the Voronoi tessellation of the electron density of the system [72].

Our initial simple decomposition scheme allows to separate the intra- and intermolecular contributions to the IR spectrum. Namely, the TCF from Eq. (1) can be rewritten as

$$\begin{aligned}\langle \boldsymbol{M}(t_0+t)\boldsymbol{M}(t_0)\rangle &= \left\langle \sum_{i=1}^{N}\boldsymbol{\mu_i}(t_0+t)\sum_{i=1}^{N}\boldsymbol{\mu_i}(t_0)\right\rangle \\ = \sum_{i=1}^{N}\left\langle \boldsymbol{\mu_i}(t_0+t)\,\boldsymbol{\mu_i}(t_0)\right\rangle &+ \sum_{i=1}^{N}\sum_{j\neq i}\left\langle \boldsymbol{\mu_j}(t_0+t)\,\boldsymbol{\mu_i}(t_0)\right\rangle,\end{aligned} \tag{2}$$

and the intra- and intermolecular terms in the IR spectrum can then be explicitly separated as,

$$\begin{aligned}\alpha(\omega) &= \mathscr{F}(\omega)\textstyle\int_{-\infty}^{\infty}\mathrm{d}t\, e^{-i\omega t}\displaystyle\sum_{i=1}^{N}\left\langle \boldsymbol{\mu_i}(t_0+t)\,\boldsymbol{\mu_i}(t_0)\right\rangle \\ &+\mathscr{F}(\omega)\textstyle\int_{-\infty}^{\infty}\mathrm{d}t\, e^{-i\omega t}\displaystyle\sum_{i=1}^{N}\sum_{j\neq i}\left\langle \boldsymbol{\mu_j}(t_0+t)\,\boldsymbol{\mu_i}(t_0)\right\rangle \\ &= \alpha_{\mathrm{mol}}(\omega) + \alpha_{\times}(\omega).\end{aligned} \tag{3}$$

In Eq. (3), the $\alpha_{\times}(\omega)$ term contains contributions from all other molecules than the tagged one. However, if a certain molecule in the system is distinguished, it is often important to know how its immediate environment modulates its IR spectrum. We may therefore demand that the dipole moment summation includes only the neighboring molecules. This approach requires the definition of a distance-dependent local dipole moment as [52],

$$\boldsymbol{\mu}_{\boldsymbol{i}}^{R}(t) = \mathscr{N}_{\boldsymbol{i}}^{R}(t)\left(\boldsymbol{\mu_i}(t) + \sum_{j\neq i}P_{ij}(t)\boldsymbol{\mu_j}(t)\right), \tag{4}$$

where $P_{ij}(t)$ is a cutoff function ensuring the continuity of the dipole moment of the jth molecule when crossing the boundary of a sphere with radius R_c and center in the center of mass (CoM) of the distinguished molecule i, while $\mathcal{N}_i^{\mathrm{R}}(t)$ is the normalization factor (normalizing the IR intensity to a single absorbing molecule). The cutoff function is a logistic function,

$$P_{ij}(t) = \left\{1 + \exp\left[\left(R_{ij}(t) - R_c\right)D^{-1}\right]\right\}^{-1}, \tag{5}$$

where $R_{ij}(t)$ is the CoM separation of molecules i and j at time t. This function selects in a continuous manner the molecules j contained within the sphere with radius R_c, wherein $P_{ij}(t) = 1$ for $R_{ij}(t) \ll R_c$ and $P_{ij}(t) = 0$ for $R_{ij}(t) \gg R_c$. The width of the transition between the two limiting values is governed by the sharpness parameter D. The normalization factor is taken as,

$$\mathcal{N}_i^{\mathrm{R}}(t) = \left(1 + \sum_{j \neq i} P_{ij}^2(t)\right)^{-0.5}. \tag{6}$$

Finally, Eq. (4) allows for a definition (summing over identical reference molecules) of the distance-dependent absorption coefficient as,

$$\alpha^{\mathrm{R}}(\omega, R_c) = \mathscr{F}(\omega) \sum_{i=1}^{N} \int_{-\infty}^{\infty} \mathrm{d}t\, \mathrm{e}^{-i\omega t} \left\langle \boldsymbol{\mu}_{\boldsymbol{i}}^{R}(t_0 + t)\, \boldsymbol{\mu}_{\boldsymbol{i}}^{R}(t_0) \right\rangle. \tag{7}$$

The limiting values of the normalization factor $P_{ij}(t)$ guarantee that Eq. (7) possesses two important limits: (1) when $R_c \to 0$, then $\alpha^{\mathrm{R}}(\omega, R_c) \to \alpha_{\mathrm{mol}}(\omega)$ and (2) when $R_c \to \infty$, then $\alpha^{\mathrm{R}}(\omega, R_c) \to \alpha(\omega)$. However, in the most interesting intermediate regime, where R_c is on the order of intermolecular separation in the liquid, $\alpha^{\mathrm{R}}(\omega, R_c)$ probes distinct responses of successive solvation shells of the tagged molecule.

The distance-dependent IR spectrum can display variable signal modulations with increasing R_c depending on the chosen probing frequency ω_p. Therefore, different fundamental bands of the studied liquid show sometimes divergent IR response modulation [52]. In search for the common trends in $\alpha^{\mathrm{R}}(\omega_p, R_c)$ at selected probing frequencies corresponding to the positions of the fundamental bands of DMSO, we apply here the techniques of the generalized 2D correlation spectroscopy, as outlined in Ref. [66]. Namely, we calculate and analyze the synchronous and asynchronous 2D correlation spectra as,

$$\Phi(\omega_1, \omega_2) = \frac{1}{r-1} \tilde{\boldsymbol{\alpha}}^{R}(\omega_1)^{T} \tilde{\boldsymbol{\alpha}}^{R}(\omega_2), \tag{8}$$

$$\Psi(\omega_1, \omega_2) = \frac{1}{r-1} \tilde{\boldsymbol{\alpha}}^{R}(\omega_1)^{T} \boldsymbol{N_r} \tilde{\boldsymbol{\alpha}}^{R}(\omega_2), \tag{9}$$

respectively, where $\tilde{\boldsymbol{\alpha}}^{R}(\omega_p)$ is a vector constructed from the distance-dependent IR spectra at the probing frequency ω_p and at r discrete increasing R_c values, while $\boldsymbol{N_r}$ is the Hilbert–Noda transformation matrix of rank r [66].

The physical significance of the $\Phi(\omega_1, \omega_2)$ intensity lies in representing the coincidental changes of two discrete spectral intensity variations observed at ω_1 and ω_2 within the studied range of the external variable (here, the cutoff radius). On the other hand, the asynchronous intensity $\Psi(\omega_1, \omega_2)$ represents out of phase spectral intensity changes at ω_1 and ω_2, thus providing useful information on the sequential order of events observed by the spectroscopic technique along the external variable.

The synchronous and asynchronous spectral maps reveal the existence of correlations and anticorrelations between different vibrational excitations, but lack direct information about coupling of vibrational response to the underlying perturbation variable. Whenever such information is desired, the spectral analysis by the moving-window two-dimensional (MW2D-COS) correlation spectroscopy [73,74] can be used to visualize a spectral map spanning the frequency and external variable axes, as opposed to the frequency vs frequency spectrum obtained in generalized 2D-COS. In a nutshell, the idea of this method is the calculation of the power spectrum $\Phi(\omega, \omega)$, i.e., the diagonal of the synchronous correlation spectrum, based not on the entire data set, but on a moving window selected along the perturbation direction. The projection of the power spectrum of a windowed data set vs the external variable gives rise to the MW2D-COS intensity map,

$$\Phi_{\mathrm{A}}(\omega, R_{c,i}) = \frac{1}{2m} \sum_{j=i-m}^{i+m} \alpha^{\mathrm{R}}(\omega, R_{c,j})^2, \tag{10}$$

calculated in a window of $2m + 1$ spectra. Generally, the MW2D-COS intensity is proportional to the squared perturbation derivative [75],

$$\Phi_{\mathrm{A}}(\omega, R_c) \propto \left[\frac{\partial \alpha^{\mathrm{R}}(\omega, R_c)}{\partial R_c}\right]^2. \tag{11}$$

Consequently, it is always positive and is particularly well suited to analyze peak shifts in IR spectra, also in the case of non-linear response to the external variable.

The nature of spectral changes around the distinguished molecule may be represented from a conceptually different approach by abandoning the discrete total dipole partitioning as in Eq. (2) and instead projecting the total dipole moment on a regular spatial grid $\boldsymbol{r}$ using a continuous dipole density,

$$\boldsymbol{\rho}_{\mu}(t, \boldsymbol{r}) = \sum_{i=1}^{N} \boldsymbol{\mu}_{\boldsymbol{i}}(t) \frac{1}{(2\pi\sigma^2)^{1.5}} \exp\left[-\frac{(\boldsymbol{R}_{\boldsymbol{i}}(t) - \boldsymbol{r})^2}{2\sigma^2}\right], \tag{12}$$

where $\boldsymbol{R}_{\boldsymbol{i}}(t)$ is the CoM position of molecule i at time t and σ is the standard deviation of the three-dimensional (3D) Gaussian projection of the molecular dipoles on the grid [51,52]. The total dipole moment may then be recovered by integration, $\boldsymbol{M}(t) = \int \mathrm{d}^3\boldsymbol{r}\, \boldsymbol{\rho}_{\mu}(t, \boldsymbol{r})$. By choosing the origin of the grid at the CoM of a tagged molecule, fixing the local molecular reference frame, and summing over equivalent solvent molecules, we may write by analogy to Eq. (2),

$$\begin{aligned} \langle \boldsymbol{M}(t_0 + t) \boldsymbol{M}(t_0) \rangle &= \left\langle \sum_{i=1}^{N} \boldsymbol{\mu}_{\boldsymbol{i}}(t_0 + t) \sum_{i=1}^{N} \boldsymbol{\mu}_{\boldsymbol{i}}(t_0) \right\rangle = N \left\langle \sum_{i=1}^{N} \boldsymbol{\mu}_{\boldsymbol{i}}(t_0 + t)\, \boldsymbol{\mu}_{\mathrm{ref}}(t_0) \right\rangle \\ &= \boldsymbol{N} \left\langle \int \mathrm{d}^3\boldsymbol{r}\, \boldsymbol{\rho}_{\mu}(t_0 + t, \boldsymbol{r})\, \mu_{\mathrm{ref}}(t_0) \right\rangle. \end{aligned} \tag{13}$$

Using this smoothly spatially decomposed total dipole moment TCF in Eq. (1) leads to,

$$\begin{aligned} \alpha(\omega) &= \mathscr{F}(\omega)\, N \int_{-\infty}^{\infty} \mathrm{d}t\, \mathrm{e}^{-i\omega t} \left\langle \int \mathrm{d}^3\boldsymbol{r}\, \boldsymbol{\rho}_{\mu}(t_0 + t, \boldsymbol{r})\, \boldsymbol{\mu}_{\mathrm{ref}}(t_0) \right\rangle \\ &= \int \mathrm{d}^3\boldsymbol{r}\, \mathscr{F}(\omega)\, N \int_{-\infty}^{\infty} \mathrm{d}t\, \mathrm{e}^{-i\omega t} \left\langle \rho_{\mu}(t_0 + t, \boldsymbol{r})\, \boldsymbol{\mu}_{\mathrm{ref}}(t_0) \right\rangle \\ &= \int \mathrm{d}^3\boldsymbol{r}\, \alpha(\omega, \boldsymbol{r}), \end{aligned} \tag{14}$$

where the spatially resolved IR spectrum, $\alpha(\omega, \boldsymbol{r})$, enables detailed analysis of the correlated oscillations of molecular dipoles in the studied liquid from the point of view of a reference molecule. The resulting spectral intensity at $\boldsymbol{r}$ can be positive, indicating locally correlated oscillations of the molecular dipole density which lead to increased IR absorption by the sample, as well as negative, signifying locally out-of-phase oscillations which contribute to decreased IR absorption [51].

The discussed concept is distinctly related to the spatial correlations in the atomic density as observed in the spatial distribution function (SDF) [76],

$$N(\boldsymbol{r}) = \rho \int \mathrm{d}^3\boldsymbol{r}\, g(\boldsymbol{r}), \tag{15}$$

that is also defined in the local molecular reference frame. Analysis in terms of SDFs provides valuable insight into the structure of molecular liquids [77,76,78].

Computational Methods

Static density functional theory (DFT) calculations were performed with the ORCA program system (v. 3.0.3) [79]. The standard BLYP functional [80,81] augmented with the empirical DFT-D3 dispersion correction [82] was applied, together with the def2-TZVPP basis set [83,84]. Tight energetic criteria were imposed throughout (10^{-8} hartree for the self consistent field convergence and 10^{-6} hartree for the geometry optimization). The geometry optimization of a DMSO monomer was followed by standard vibrational analysis via Hessian diagonalization.

AIMD simulations [57] were performed following the protocol previously established for liquid GBL [56,55]. The simulations were carried out using the QUICKSTEP electronic structure module [85] based on DFT and implemented in the CP2K package (v. 2.7) [86,87]. We used the BLYP functional [80,81] together with the DFT-D3 empirical dispersion correction [82] in order to better account for dispersion interactions in the liquid. QUICKSTEP is based on a combined Gaussian atomic orbitals with plane waves (GPW) representation of the electronic structure [88] and we used a TZV2P basis set for atomic orbitals coupled with the auxiliary plane wave expansion up to a 500 Ry cutoff. Core electrons were represented by norm-conserving GTH pseudo potentials [89]. The cutoff for the DFT-D3 correction was set to 18 Å.

The studied system was composed of 38 DMSO molecules and was contained in a cubic cell with periodic boundary conditions imposed and with edge length set to reproduce the experimental density of the liquid at $T = 298.15$ K (1095.2 kg m^{-3} [10]), that is $L \approx 16.51$ Å. The starting molecular configuration was generated using PACKMOL [90]. The system was initially equilibrated in the canonical (*NVT*) ensemble for 25 ps with a time step of 0.5 fs using massive Nosé–Hoover chain thermostatting for temperature stabilization [91]. The time constant of the thermostat was set to 2000 cm^{-1} (≈ 16.67 fs). An elevated temperature, $T = 360$ K, was used to mimic liquid dynamics in standard conditions. Such empirical rescaling is often applied to avoid the temperature underestimation that is usually associated with DFT-based simulations of the liquid state with GGA functionals [92,93]. This particular choice of temperature adequately reproduced liquid GBL diffusion at standard conditions [56] and also provides an excellent estimate of liquid DMSO diffusion, *vide infra.*

After the equilibration run, the canonical simulation was continued and 32 statistically independent initial conditions were subsequently sampled every 5 ps from it in order to initialize microcanonical (*NVE*) trajectories with 20 ps length each. During the *NVE* runs, the centers of maximally localized Wannier functions were computed every 4 trajectory steps (2 fs) and molecular dipole moments were obtained based on the Wannier function centers.

The distance-dependent IR spectra were calculated according to the equations presented in Section 2 using the sharpness parameter $D = 0.25$ Å and at cutoff radii $R_c = 0.1$–8.2 Å increasing in 0.1 Å steps. For the spatially resolved IR spectra, $\sigma = 0.4$ Å and a cubic grid of $31 \times 31 \times 31$ points (grid spacing $\sim$0.55 Å) were used for the dipole density projection, Eq. (12). All spectra were smoothed by passing through a Gaussian filter with 5 cm^{-1} width. Numerical Kramers–Kronig transform was applied to remove the refractive index dispersion effects in the IR spectra [94], using the experimental refractive index of DMSO, $n_\mathrm{D} = 1.4765$ [95]. In order to obtain canonical averages, all observables were averaged over the 32 *NVE* trajectories [96]. The FITYK software was used for numerical fits [97]. All isosurface plots were prepared with VMD [98].

Results and discussion

Structure and dynamics of liquid DMSO

The structure of liquid DMSO is well known from diffraction experiments [14–17]. In order to assess the accuracy of the present simulations, we compare the most important intra- and intermolecular distances to the recent experimental data in Table 1. Our results are clearly in excellent agreement with experiment, with the two notable exceptions of the $\mathrm{C}\cdots\mathrm{O}$ and $\mathrm{O}\cdots\mathrm{H}$ pairs. However, the $\mathrm{C{-}H}\cdots\mathrm{O}$ contacts, albeit weakened, are still important in the simulated liquid, as discussed below. Overall, the DMSO molecule displays a trigonal pyramidal structure (C_s point group), in accordance with numerous experimental and computational studies [18–20,14–17]. The average CSC angle is 96.5°, while the CSO angles are 106.5°.

Most notably, the MLWF representation of the electronic structure delivers an elegant pedagogical illustration of the strongly polarized character of the $\mathrm{S}^{+}\!\rightarrow\!\mathrm{O}^{-}$ bond and the sp^3 hybridization of sulfur, see Fig. 1. The single bond character of the S—O bond is supported by natural bond orbital (NBO) analysis [20]. The sp^3 hybridization of both S and O atoms was previously found in MLWF analysis of DMSO–water clusters [64]. The strong polarization of the S—O bond gives rise to a considerable dipole moment of liquid DMSO. The gas phase monomer value (3.96 D [8]) is substantially increased to 5.72 D in our simulations, where the molecular dipole moment distribution is Gaussian with a standard deviation equal to 0.48 D. We note here that water induces even stronger polarization and raises the dipole moment of hydrated DMSO up to 7.4 D [64,63]. Another notable feature seen in Fig. 1 is the relative rotational freedom of the methyl groups (evident from the spread of the lobes representing the C—H bonding orbitals). However, the hydrogen atoms are seen to not rotate completely freely, but rather in jumps about three equivalent sites, as inferred previously from neutron diffraction data [16].

Cyclic hydrogen bonded (H-bonded) dimers are well known to be the most stable molecular arrangements in $(\mathrm{DMSO})_2$ [18–20,15]. As noticed above, the $\mathrm{O}\cdots\mathrm{H}$ intermolecular distance has on average $\sim$0.3 Å higher value in the present AIMD simulations than in experiment [15] suggesting that the $\mathrm{C{-}H}\cdots\mathrm{O}$ hydrogen bond contacts are slightly weakened. Nevertheless, the potential well for the possible H-bonds is certainly present in our simulations as evident from Fig. 2, where a 2D radial distribution function (RDF), $g(r,\beta)$, in the plane spanned by the intermolecular $\mathrm{C}\cdots\mathrm{O}$ distance and the angle between the $\mathrm{C}\cdots\mathrm{O}$ and C—H vectors is shown. The 2D RDF contour is directly transferable to the potential of mean force (PMF) for the respective interaction *via* [99],

$$W(r,\beta) = -k_\mathrm{B}T \ln g(r,\beta), \tag{16}$$

so that the isolines in Fig. 2 show the underlying PMF measured in units of thermal energy $k_\mathrm{B}T$. The global minimum of the PES is $-2.3k_\mathrm{B}T$ and there is a sizable basin where the attractive potential is greater than the thermal energy at $r < 3.9$ Å and $\beta < 35^\circ$. Accordingly, we define a smooth contour—a combination of two ellipses with different semi-minor axes—that delineates the region of H-bond existence. Note that since we only consider configurations more stable than $k_\mathrm{B}T$ we effectively count "thermally stable" H-bonds only.

Table 1
The comparison of AIMD simulations results with the experimentally determined mean bond distances (r/ Å) and coordination numbers (N) in liquid DMSO.

Pair	AIMD (this work)		Experimental [15]	
	r	N	r	N
Intramolecular				
S=O	1.53	1.0	1.52	1.0
S—C	1.85	2.0	1.85	2.0
C—H	1.09	3.0	1.07	3.0
O⋯C	2.73	2.0	2.61	2.0
C⋯C	2.77	1.0	2.68	1.0
Intermolecular				
S⋯S	5.29	13.6	5.26	13.8
S⋯O	4.57	4.9	4.58	5.1
C⋯S	4.27	3.5	4.07	3.5
C⋯O	3.39	2.7	2.96	3.0
O⋯H	2.47	4.3	2.15	3.0

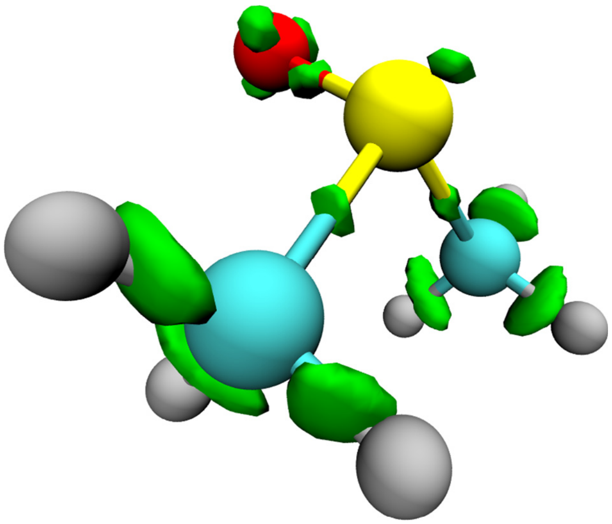

Fig. 1. Average internal structure of a DMSO molecule in liquid DMSO: red – oxygen, yellow – sulfur, cyan – carbon, and gray – hydrogen. The green lobes show the spatial distribution of the MLWF centers in the reference frame defined by the molecule. (For interpretation of the references to colour in this figure legend, the reader is referred to the web version of this article.)

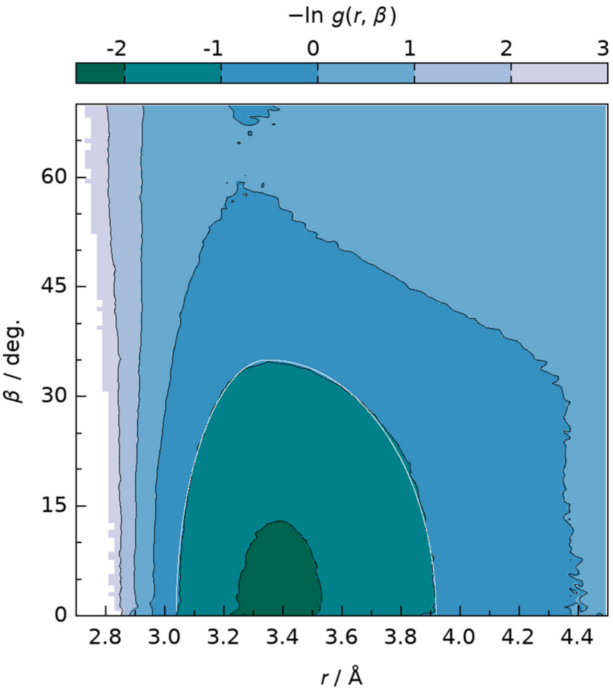

Fig. 2. Two-dimensional radial distribution function, $g(r,\beta)$, in liquid DMSO for r equal to the intermolecular C. . .O distance and β equal to the angle between the C. . .O and C-H vectors, plotted on a logarithmic scale as $-\ln g(r,\beta)$. Thin white line denotes the smooth cutoff region for C-H. . .O hydrogen bond existence.

Even though the accepted criteria are quite strict, the degree of instantaneous hydrogen bonding in liquid DMSO is considerable. On average, every O atom accepts 1.74 H-bonds. However, the fraction of 3- or even 4-coordinated oxygens is non-negligible, as clearly seen in Fig. 3. This further suggests that an extensive network of C—H⋯O H-bonds governs the local ordering in liquid DMSO. In order to picture also the dynamical nature of this H-bonded network, we resort to the continuous hydrogen bond correlation function that can deliver the lower bound of the mean H-bond persistence time [100]. Briefly, let us define an H-bond population operator, $h(t)$, that is equal to 1 if a particular tagged pair of DMSO molecules is H-bonded at time t and 0 otherwise. Simultaneously, its continuous counterpart, $H(t)$, is equal to 1 only if the tagged pair is H-bonded *continuously* in the time period $[0;t]$. The latter operator lets us define a TCF, $C(t)$, the integral of which evaluates to the above-mentioned mean H-bond persistence time as [100],

$$\tau_{\mathrm{HB}} = \int_0^\infty \mathrm{d}t\, C(t) = \int_0^\infty \mathrm{d}t\, \langle h(0)H(t)\rangle / \langle h\rangle, \tag{17}$$

where $\langle\ldots\rangle$ denotes an ensemble average over all bonds present at time $t = 0$. The $C(t)$ function for the studied system is shown in Fig. 3 and the average value of the resulting H-bond persistence time for liquid DMSO obtained from Eq. (17) is 0.12 ps. Even though by definition it is the lower bound of the true H-bond lifetime [100] and the employed H-bond existence criteria are quite strict, it is still an order of magnitude longer than the characteristic time of the $\nu_{\mathrm{C-H}}$ stretching vibration located at 3000 cm^{-1} [33,34]. Consequently, the H-bonds are expected to be long-lived enough to alter the IR response in the $\nu_{\mathrm{C-H}}$ range.

Finally, to gain confidence that our increased temperature simulations really represent liquid DMSO at ambient conditions, we estimate its self-diffusion coefficient from the Einstein relation,

$$D = \frac{1}{6}\lim_{t\to\infty}\frac{\langle\Delta r^2(t)\rangle}{t}, \tag{18}$$

where $\Delta r^2(t) = |\mathbf{r}(t) - \mathbf{r}(0)|^2$ is the mean square displacement (MSD) of the molecular center of mass. While AIMD simulations are frequently too short to reliably estimate the self-diffusion coefficients of liquids [101], taking advantage of the long aggregated simulation time in the present study allows us to reliably estimate the value of D, as evidenced by the time evolution of the right hand

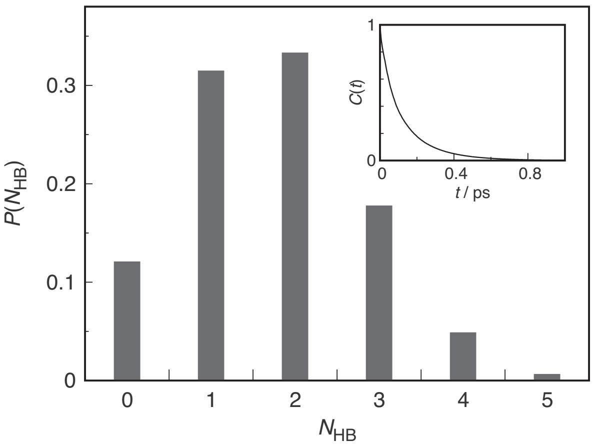

Fig. 3. Instantaneous hydrogen bond number distribution calculated by counting the number of C–H···O hydrogen bonds per oxygen atom according to the geometric criteria as shown in Fig. 2. (inset) The time correlation function of the continuous hydrogen bond population operator.

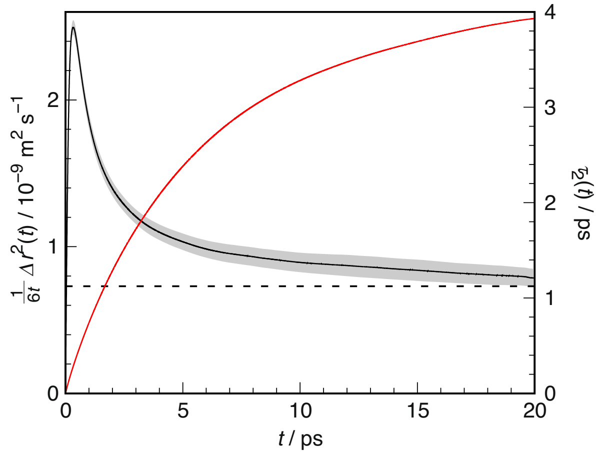

Fig. 4. The time evolution of the time-scaled mean square displacement of the DMSO molecule in liquid DMSO (black, left ordinate) and its 95% confidence interval (shaded area). Black dashed line indicates the experimental value ($0.73 \cdot 10^{-9}$ m^2 s^{-1} [102]). Also shown is the time evolution of the integration of the second rank orientational correlation function of the S=O vector in the DMSO molecule (red, right ordinate). (For interpretation of the references to colour in this figure legend, the reader is referred to the web version of this article.)

side of Eq. (18) which is plotted in Fig. 4. The limiting value of the self-diffusion coefficient seems to have been reached, indicating that our sampling is long enough to give meaningful statistics. The converged value, $D = (0.79 \pm 0.06) \cdot 10^{-9}$ m^2 s^{-1}, is in excellent agreement with the experimental one, $0.73 \cdot 10^{-9}$ m^2 s^{-1} [102]. Thus, the translational mobility of DMSO molecules is fully representative of the liquid at ambient conditions.

Another important parameter reflecting the mobility of the liquid molecules is the rotational correlation time, which was extensively studied for liquid DMSO, both experimentally and computationally (see Ref. [23] for a review). Orientational relaxation is described by the TCF of molecular orientation,

$$C_l(t) = \langle P_l[\boldsymbol{u}(0)\boldsymbol{u}(t)]\rangle, \tag{19}$$

where P_l is the Legendre polynomial of rank l and $\boldsymbol{u}$ is a unit vector along the chosen molecular axis [23]. In particular, $l = 2$ is relevant for comparison with NMR experiments. The second rank rotational correlation time is then obtained by integration, $\tau_2 = \int_0^\infty \mathrm{d}t\, C_2(t)$. The time evolution of the respective integral is shown in Fig. 4, where $\boldsymbol{u}$ has been chosen to be the direction of the S=O vector in the DMSO molecule. While it is apparent that the limiting value of τ_2 has not yet been reached on the time scale of the present simulations, our tentative estimate of ~4 ps (assuming exponential rise to the limiting value) appears to be in good agreement with NMR measurements that yield 5.2 ps for ^{17}O and 3.7 ps for ^{33}S [103]. Most computational predictions give values in this range [23]. Therefore, we may be reasonably confident that not only translational, but also rotational mobility of liquid DMSO is faithfully captured by our AIMD simulations, which is an excellent predictor for the validity of the more intricate IR spectra decompositions that follow.

Distance-dependent modulation of IR spectrum of liquid DMSO

In order to set the stage for the spatial decomposition schemes outlined in Section 3 we first assess the relative proportion of the intra- and intermolecular terms in the IR spectrum, cf. Eq. (3). As seen in Fig. 5, the contribution of the $\alpha_\times(\tilde{\nu})$ term is certainly non-negligible and amounts to ~30% of the total IR intensity across the mid-IR range, even more than in the case of GBL [55]. Although in contrast to liquid water [52,51] no band shape changes or position shifts are immediately noticeable between $\alpha_{\mathrm{mol}}(\tilde{\nu})$ and the bulk IR spectrum, the intensity increase that must be accounted for by the intermolecular spectrum is nevertheless substantial.

To facilitate easier comparison with available experimental data and simplify the discussion, we assigned the bands visible in the calculated IR spectrum to the fundamental vibrations of DMSO, based on proximity to experimental bands and relative intensity, see Table 2. Although the bands in the computed IR spectrum are displaced with respect to the experimental ones, the magnitude of the error is well within the limits of AIMD investigations of IR spectra with GGA-based functionals [55,104]. Note that the spectra shown in Fig. 5 have been scaled neither by any empirical scale factor nor by an intensity multiplier.

The distance-dependent IR spectra observed from the point of view of a tagged molecule in an isotropic liquid illustrate, how the IR response changes from the purely intramolecular contribution up to the bulk limit [52]. They can also unravel the details of the characteristic spectral influence of the central solute on the surrounding solvent [56,94]. The distance-dependent spectra at

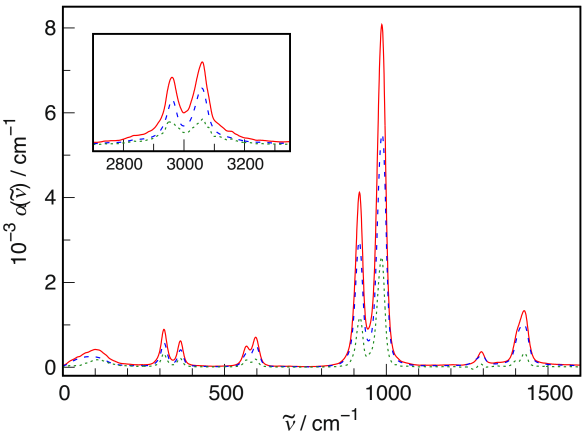

Fig. 5. IR spectrum of liquid DMSO (red solid line), decomposed into the intramolecular (blue dashed line) and intermolecular (green dotted line) terms, $\alpha_{\mathrm{mol}}(\tilde{\nu})$ and $\alpha_\times(\tilde{\nu})$, respectively. Inset shows the C–H stretching vibrations region. (For interpretation of the references to colour in this figure legend, the reader is referred to the web version of this article.)

Table 2

Calculated and experimentally observed fundamental IR frequencies ($\tilde{\nu}$/ cm^{-1}) and the band assignments for liquid DMSO

Assignment[a]	AIMD (this work)	Experimental [33]
$\nu^{s}_{\mathrm{C-H}}, \nu^{a}_{\mathrm{C-H}}$	2960, 3060	2905, 2991
$\delta^{a}_{\mathrm{CH_3}}$	1425	1419
$\delta^{s}_{\mathrm{CH_3}}$	1295	1311
$\nu_{\mathrm{S=O}}$	985	1070
$\rho_{\mathrm{CH_3}}$	915	1032
$\nu^{s}_{\mathrm{C-S-C}}, \nu^{a}_{\mathrm{C-S-C}}$	570, 595	670, 700
$\delta_{\mathrm{C-S-C}}$	365	383
$\tau_{\mathrm{C-S-C}}$	315	335
Network modes	100	—

[a] Notation: $\nu^{s}_{\mathrm{C-H}}, \nu^{a}_{\mathrm{C-H}}$ – symmetric and asymmetric stretching mode of CH$_3$ groups, $\delta^{a}_{\mathrm{CH_3}}, \delta^{s}_{\mathrm{CH_3}}$ – asymmetric bending and umbrella mode of CH$_3$ groups, $\nu_{\mathrm{S=O}}$ – S=O stretching mode, $\rho_{\mathrm{CH_3}}$ – rocking mode of CH$_3$ groups, $\nu^{s}_{\mathrm{C-S-C}}, \nu^{a}_{\mathrm{C-S-C}}$ – symmetric and asymmetric C-S-C stretching mode, $\delta_{\mathrm{C-S-C}}, \tau_{\mathrm{C-S-C}}$ – C-S-C bending and twisting modes [33].

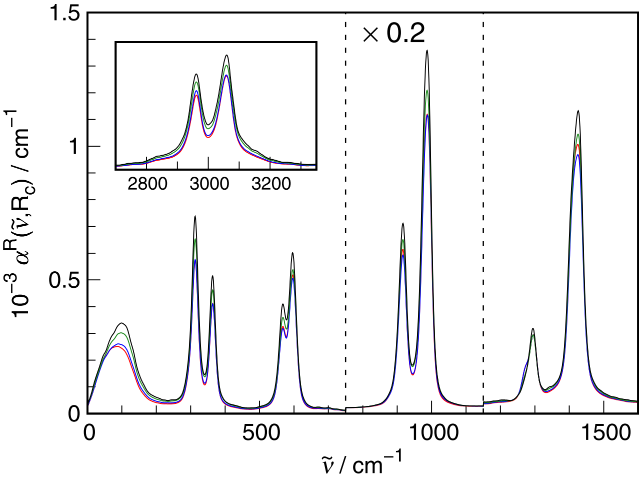

Fig. 6. Distance-dependent IR spectrum of liquid DMSO shown for $R_c = 2$ Å (red), 4 Å (blue), 6 Å (green) and 8 Å (black). Spectral intensity in the range of $\nu_{\mathrm{S=O}}$ and $\rho_{\mathrm{CH_3}}$ fundamental vibrations was scaled by 0.2 to facilitate comparison of different spectral regions. Inset shows the C-H stretching vibrations region. (For interpretation of the references to colour in this figure legend, the reader is referred to the web version of this article.)

selected cutoff radii—measured from the CoM of the distinguished molecule as defined in Eq. (4)—are presented in Fig. 6.

It is readily visible that the spectral intensity at any probe wavenumber $\tilde{\nu}$ generally increases with the cutoff radius R_c. However, this modulation is often non-monotonous and can vary between different spectral regions. Exemplary dependences of the $\alpha^{\mathrm{R}}(\tilde{\nu}, R_c)$ spectrum on R_c at probe wavenumbers corresponding to the important bands of liquid DMSO (cf. Table 2) are shown in Fig. 7. A quick comparison to the course of the CoM–CoM RDF included in the figure reveals that the distance-dependent IR spectrum is most heavily modulated by the reference molecule's nearest neighbors. The monotonously increasing C—H stretching band intensity is rather an exception, as most bands in the spectrum are characterized by a prominent dip in spectral intensity at $R_c \approx 4.5$ Å.

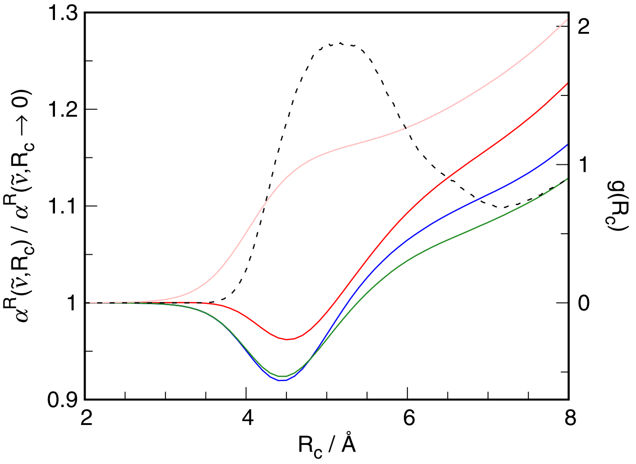

Fig. 7. The modulation of the distance-dependent IR spectrum of liquid DMSO with increasing cutoff distance for the $\nu_{\mathrm{S=O}}$ (red), $\rho_{\mathrm{CH_3}}$ (blue), $\delta^{a}_{\mathrm{CH_3}}$ (green), and $\nu^{s}_{\mathrm{C-H}}$ (pink) bands. Spectral intensity at each R_c is scaled by the intensity at $R_c \to 0$ (i.e., the single molecule limit of the IR spectrum). See Table 2 for band assignments. The radial distribution function based on the center of mass separation between DMSO molecules (black dashed line, right ordinate) is shown for reference. (For interpretation of the references to colour in this figure legend, the reader is referred to the web version of this article.)

In order to disentangle the mutual relations between the band intensities, we apply the principles of generalized 2D-COS [66] to the spectral series of $\alpha^{\mathrm{R}}(\tilde{\nu}, R_c)$ spectra with increasing R_c. The resulting spectral intensity maps up to 1600 cm^{-1} are shown in Fig. 8. Since the spectra shown in Fig. 8 are dominated by the $\nu_{\mathrm{S=O}}$ and $\rho_{\mathrm{CH_3}}$ auto- and cross-correlations, in the Supplementary Material we additionally offer the same figure, but with the two mentioned bands removed and the other signals artificially enhanced in order to aid in the discussion of the respective correlation peaks (see Fig. S1). The correlations maps involving the C-H stretching vibrations are likewise shown in the Supplementary Material (see Fig. S2 and S3 for near-diagonal and off-diagonal correlations, respectively). Because the meaning of positive and negative correlations in the synchronous spectra differs from the asynchronous ones, we discuss these cases separately.

When looking at the synchronous spectrum of liquid DMSO, one immediately sees that the $\nu_{\mathrm{S=O}}$ and $\rho_{\mathrm{CH_3}}$ bands dominate the autocorrelation spectrum on the diagonal line. This is simply related to their much higher intrinsic intensity as compared to other bands in the IR spectrum (cf. Fig. 5). Similarly, the vast majority of the off-diagonal peaks also show positive intensity. This generally means that the spectral intensity at the two given wavenumbers changes in a synchronous manner [66]. One very important exception is the $\delta^{s}_{\mathrm{CH_3}}$ umbrella mode, which is consistently negatively correlated with all other spectral signals. This desynchronized nature of the distance modulation of the umbrella mode is unique among the observed bands. Apparently, the intramolecular contribution (i.e., the $\alpha_{\mathrm{mol}}(\tilde{\nu})$ spectrum) responds very differently to intermolecular interactions in this spectral range than in all other ranges.

Examination of the synchronous correlations involving the $\nu_{\mathrm{C-H}}$ stretching vibrations leads to similar conclusions. The off-diagonal correlations with the lower frequency part of the IR spectrum reveal overwhelmingly positive signals with the sole exception of the cross-correlation with the $\delta^{s}_{\mathrm{CH_3}}$ band (see Fig. S3). On the other hand, the synchronous 2D-COS spectrum within the $\nu_{\mathrm{C-H}}$ range itself is reminiscent of the case of two coupled bands which intensity co-evolves in a correlated manner (see Fig. S2) [105].

Furthermore, several pairs of closely located bands are seen to be strongly correlated as evidenced by the presence of well defined correlation squares in the synchronous spectrum. This concerns in particular the $\delta_{\mathrm{C-S-C}} + \tau_{\mathrm{C-S-C}}$, $\nu^{s}_{\mathrm{C-S-C}} + \nu^{a}_{\mathrm{C-S-C}}$ and, most notably, the $\nu_{\mathrm{S=O}} + \rho_{\mathrm{CH_3}}$ pairs (see Fig. S1 in the Supplementary Material for an overview of the fine details of the weaker intensity parts of 2D-COS spectra). Moreover, the $\delta^{a}_{\mathrm{CH_3}}$ band reveals a hidden structure composed of at least two component bands as evidenced by the underlying correlation square in the synchronous spectrum. The shape of

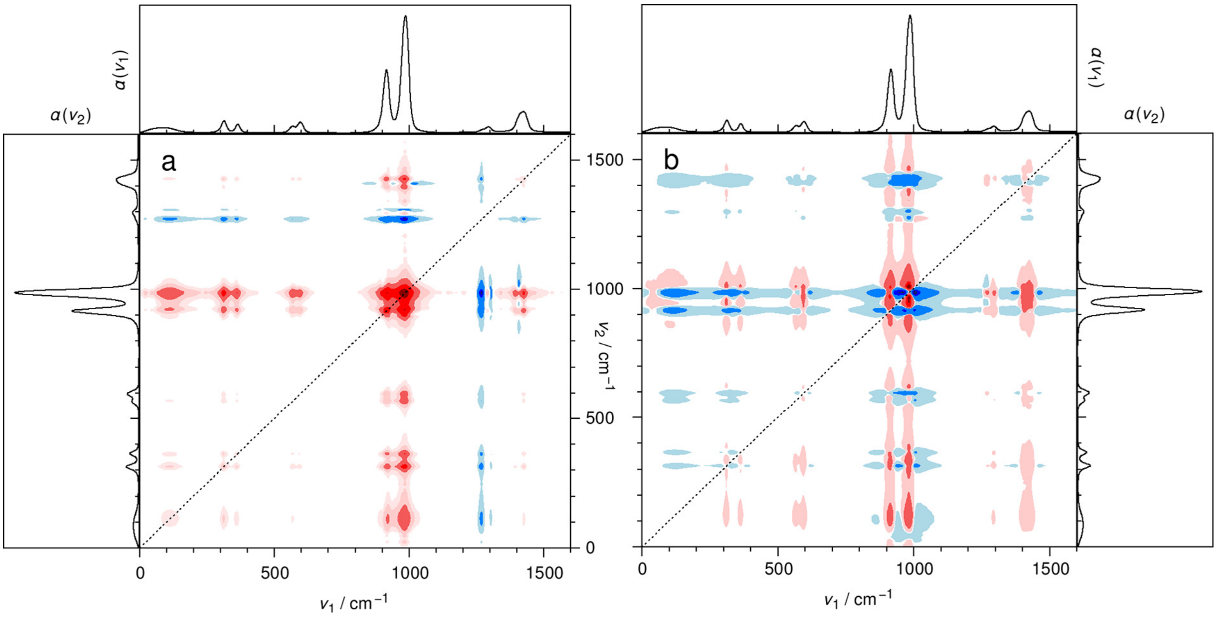

Fig. 8. (a) Synchronous and (b) asynchronous 2D IR correlation spectra based on distance-dependent IR spectra of liquid DMSO for R_c = 0.1–8.2 Å. Red shades denote positive intensity, while negative intensity is shown in blue shades. The top and side panels show the spectrum for $R_c \to 0$ (i.e., the single molecule limit) for reference. (For interpretation of the references to colour in this figure legend, the reader is referred to the web version of this article.)

the $\delta^{s}_{\mathrm{CH_3}}$ region is also non-trivial. The interpretation of these observations is discussed below, based on further data from the asynchronous spectrum.

In contrast to the synchronous spectrum, the asynchronous one can reveal the order of the changes in different spectral signals observed with the changing external variable (here, the cutoff distance) [66]. It can also help identify the common spectral patterns (such as band broadening or shifting) that frequently underlie the complex signals detected in IR spectra [66,105].

We begin the discussion of the asynchronous spectrum with the analysis of the umbrella mode correlations, due to its unique character found in the synchronous spectrum. While the synchronous cross-correlation peaks are consistently negative, the asynchronous ones at $\tilde{\nu}_1 = 1295$ cm^{-1} are uniformly positive across the mid-IR range. According to the sign conventions in 2D-COS, this means that intensity changes at the $\delta^{s}_{\mathrm{CH_3}}$ band lag behind the changes at other fundamental bands with increasing R_c [66]. Hence, the umbrella mode undergoes modulation that occurs at greater R_c values than for other bands. A careful inspection of the discussed band reveals also that the bulk of the correlation intensity stemming from it actually traces back to a distinct shoulder at ca. 1270 cm^{-1} that is present only in the intramolecular limit and vanishes in the $R_c \to \infty$ limit. The two sub-bands of the $\delta^{s}_{\mathrm{CH_3}}$ mode are apparently not much correlated judging from 2D-COS maps. Their identity is immediately seen from the vibrational analysis of an optimized DMSO monomer. The two normal modes (here found at 1266 and 1287 cm^{-1}) are $\mathrm{CH_3}$ umbrella modes of a different symmetry: while in the latter both $\mathrm{CH_3}$ groups of DMSO move in a symmetric, in-phase manner, in the former their movement is antisymmetric, i.e., they open and close in an out-of-phase fashion. The antisymmetric component can be observed in the single molecule limit of the IR spectrum of liquid DMSO, but its intensity gets quenched by the environment thus leaving only the symmetric umbrella mode in the bulk spectrum. This is perhaps the first observation of such phenomenon, as the reverse situation is usually encountered (cf. the appearance of the longitudinal acoustic H-bond mode in liquid water completely absent in the intramolecular limit [52]).

Similarly to the symmetric $\mathrm{CH_3}$ bending, the $\delta^{a}_{\mathrm{CH_3}}$ band also presents an interesting case. The signal in the synchronous 2D-COS spectrum at the lower wavenumber edge of the band ($\sim$ 1405 cm^{-1}) bears a characteristic mark of an underlying band width change—a central positive peak on the diagonal with four negative satellite peaks in a cross-like pattern [66] (see Fig. S1). The accompanying asynchronous signal (the so-called “rotated four-leaf clover”) is imperfect due to the coupling with the higher wavenumber edge of the band ($\sim$ 1435 cm^{-1}). The static vibrational analysis again helps to resolve the underlying phenomena. Just like the $\delta^{s}_{\mathrm{CH_3}}$ band, the $\delta^{a}_{\mathrm{CH_3}}$ one is a combination of several normal modes that represent asymmetric $\mathrm{CH_3}$ bending in which both methyl groups of DMSO move in an in-phase or out-of-phase manner. The latter mode is yet again quenched by the molecular environment, but since the two sub-bands are broader and thus more overlapped than the umbrella modes, it manifests itself as band narrowing rather than shoulder disappearance.

Further conclusions can be drawn also for the above mentioned pairs of strongly correlated nearby bands (e.g., $\nu_{\mathrm{S=O}} + \rho_{\mathrm{CH_3}}$) based on the asynchronous spectrum. They display an interesting quadruplet of cross-like intensity patterns with two positive and two negative signals each, perhaps best visible for the $\delta_{\mathrm{C-S-C}} + \tau_{\mathrm{C-S-C}}$ pair. The asynchronous cross-correlation intensity is pronounced in between the pairs of the strongly correlated bands rather than at the positions of the cross peaks found in the synchronous spectrum (cf. Figs. 8 and S1), so that each auto peak and each cross peak shows a distinct pattern with the same features (i.e., a cross-like quadruplet), leading to the overlap of signals originating from the auto and cross peaks. A similar, although heavily distorted pattern is visible in the asynchronous correlation between the two $\nu_{\mathrm{C-H}}$ bands of different symmetry, cf. Fig. S2. Since this kind of 2D-COS pattern is not widely discussed in the literature of the subject [66,105], we analyze it with more scrutiny in order to detect the underlying cause leading to these particular intensity maps—see Supplementary Material for an in-depth documentation of this analysis, described in the following.

The model study is based on the aforementioned $\delta_{\mathrm{C-S-C}} + \tau_{\mathrm{C-S-C}}$ pair of closely located and strongly coupled bands. In order to better analyze the changes in the spectra in this particular range, an attempt was made to approximate the $\alpha^{R}(\tilde{\nu}, R_c)$ spectral series with an analytical curve. It turns out that the distance-dependent spectra at all R_c are faithfully represented by two Pearson type VII profiles with a minimal fit residue (see Fig. S4). The decomposition of the spectra into analytical bands enables a judicious examination of the change of their parameters with increasing R_c, as seen in Fig. S5. It turns out that the integral intensity of both bands raises in an almost concerted manner starting at $R_c \approx 3.5$ Å and up to the system size limit. On the other hand, the position at maximum of these bands shows three distinct regimes: the short range one (up to $R_c = 2.5$ Å), in which it remains fixed for both analytical profiles as the spectrum is clearly dominated by the intramolecular response of the reference molecule, the mid-range one (R_c = 2.5–5.3 Å), in which the trends in the position shift are mostly opposing, and finally the long range one ($R_c > 5.3$ Å), where a concerted redshift of positions at maximum can be observed. As seen in Fig. S6 the reconstructed spectral series based on the analytical profiles faithfully represents the shape of 2D-COS patterns observed based on original data (cf. Fig. S1). However, the above proposed separation of the distance regimes traces the observed patterns in the synchronous and asynchronous spectra to different underlying phenomena. As seen in Figs. S7 and S8, while the synchronous spectrum pattern is determined by the mid-range part of the spectral series, the asynchronous one is in turn shaped by the long range regime. This dependence of the shape of 2D-COS spectra on the considered range of the external variable was noted previously [75]. The present very characteristic pattern in the asynchronous 2D-COS spectra—which we trace back to two bands simultaneously increasing in intensity and shifting in the same direction—can have a diagnostic meaning in the interpretation of 2D-COS spectra in general. It is prevalent in the spectra obtained here (see Fig. S1) and signifies that this particular coupling in intensity–position change is common in closely located and strongly coupled vibrational modes in liquid DMSO.

Concluding the analysis of the distance-dependent IR spectra, we finally present the MW2D-COS intensity map constructed from them using a window of 1 Å width, see Fig. 9. It helps to identify at least three regimes in the R_c-dependence of the autocorrelation spectrum. The first one spans roughly the 3–4.7 Å range and is connected with strong intensity variations in most of the bands, notably the $\nu_{S=O} + \rho_{CH_3}$ pair, the δ_{CH_3} bands and the THz mode at $\sim$100 cm^{-1}. While such distances are at the lower limit of the first solvation shell in liquid DMSO, cf. Fig. 7, they are expected as the mean CoM to H-bond center distance in the liquid. Thus, the relatively weak C-H…O H-bonding is unsurprisingly again identified as the major driving force behind the changes in the IR spectrum across the entire mid-IR range. The second distance regime encompasses the 4.7–6.5 Å range and is connected with intensity changes in most of the bands, particularly $\nu_{S=O}$, but is virtually absent in the THz mode. This distance regime can also be viewed as the average separation between the neighboring molecules in liquid DMSO, as evidenced by the respective RDF (see Fig. 7)). At this distance regime the vibrational response is expected to be shaped by the direct dipole–dipole interactions between the neighboring molecules, leading to a general strengthening of the IR intensity. Finally, beyond the 6.5 Å boundary, the THz mode is again seen to increase its intensity, while other bands undergo further modulation with a slight intensity decrease between the first and the emergent second solvation shell of the reference molecule. While this distance regime eludes deeper analysis due to the system size limitation, we can speculate that the nascent THz intensity reflects the slowly building "mesoscopic" structure of the liquid beyond the first solvation shell [106]. This phenomenon is further analyzed below in connection to the spatially resolved IR spectrum of DMSO.

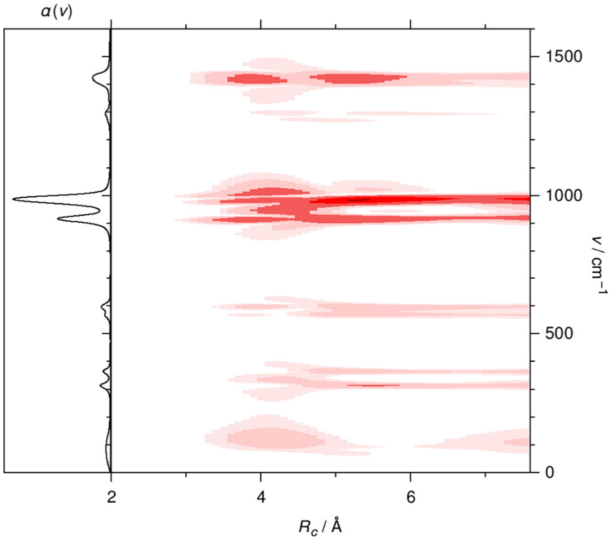

Fig. 9. Moving-window two-dimensional correlation spectrum based on distance-dependent IR spectra of liquid DMSO for R_c = 0.1–8.2 Å using a window width of 1 Å. Darkening red shades denote increasing spectral intensity. The side panel show the spectrum for $R_c \to 0$ (i.e., the single molecule limit) for reference. (For interpretation of the references to colour in this figure legend, the reader is referred to the web version of this article.)

Spatially resolved IR spectrum of liquid DMSO

As demonstrated for water [51] and other molecular liquids [55], the spatially resolved IR spectrum contributes to deeper understanding of the nature of the dipolar couplings in the system as seen from the point of view of the fixed reference molecule. By selectively probing the frequencies of the fundamental bands, a detailed picture of the intermolecular couplings in different spectral regions can be obtained, in which distinct positive and negative spatial domains observed around the reference molecule reflect the local (anti-) correlations with dipolar density in the immediate surroundings. This added depth is particularly important for anisotropic molecules with spatially varying local solvation environments [55].

The spatially resolved IR spectra of liquid DMSO at selected sampling wavenumbers (see Table 2) are shown in Fig. 10. The respective spectra for all the normal modes visible in the IR spectrum of the liquid (see Fig. 5) are shown in the Supplementary Material in Figs. S9–S11, as well as in the Supplementary Movie 1.

It is striking, how the intermolecular correlations underlying IR spectra lead to distinct positive and negative spatial domains unique to each fundamental vibration. Since the solvation environment of a reference DMSO molecule in the liquid is anisotropic, the positive and negative features observed in the spatially resolved IR spectrum may in principle correspond to specific intermolecular interactions as revealed by SDFs. However, as seen in Fig. 11, the observed spectral features do not obviously correspond to particular intermolecular contacts (see also Fig. S12 in the Supplementary Material for further SDF data).

Focusing first on the dominant bands in the IR spectrum of liquid DMSO ($\nu_{S=O}$ and ρ_{CH_3}), we find a somewhat similar picture of positive regions located above and below the reference molecule (as oriented in Fig. 10), as well as negative regions encircling the molecule that in case of $\nu_{S=O}$ coalesce into a single negative "belt". Examining the negative regions, a good degree of similarity may be found to the SDF of O atoms that are located "equatorially" around the reference molecule (see Fig. 11). On the other hand, the O atom density positioned below the reference molecule is apparently correlated with positive intermolecular IR coupling. The other promi-

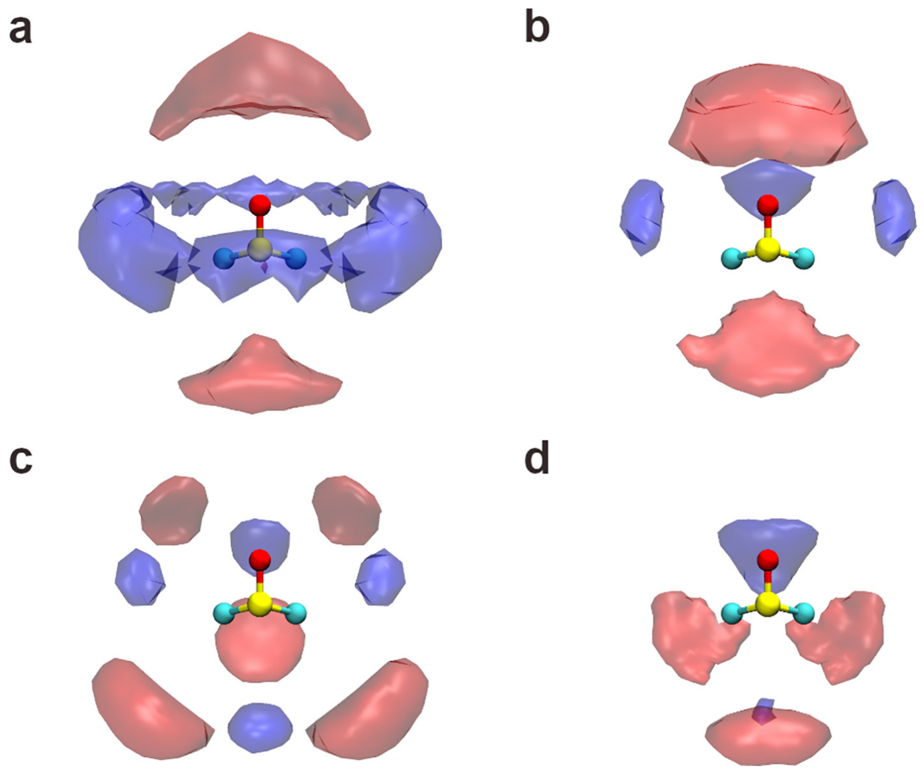

Fig. 10. Spatially resolved IR spectrum of liquid DMSO at (a) $\tilde{\nu} = 985\mathrm{cm}^{-1}$ (the $\nu_{\mathrm{S=O}}$ band), (b) $\tilde{\nu} = 915\mathrm{cm}^{-1}$ (the $\rho_{\mathrm{CH_3}}$ band), (c) $\tilde{\nu} = 1425\mathrm{cm}^{-1}$ (the $\delta^{a}_{\mathrm{CH_3}}$ band), and (d) $\tilde{\nu} = 1295\mathrm{cm}^{-1}$ (the $\delta^{s}_{\mathrm{CH_3}}$ band). The reference frame is defined by the central molecule (hydrogen atoms not shown) and the intramolecular contribution at the origin is removed for clarity. Red surfaces indicate positive correlations, while blue surfaces denote negative ones. Each isosurface is plotted at ~30% of the maximum cross correlation intensity.

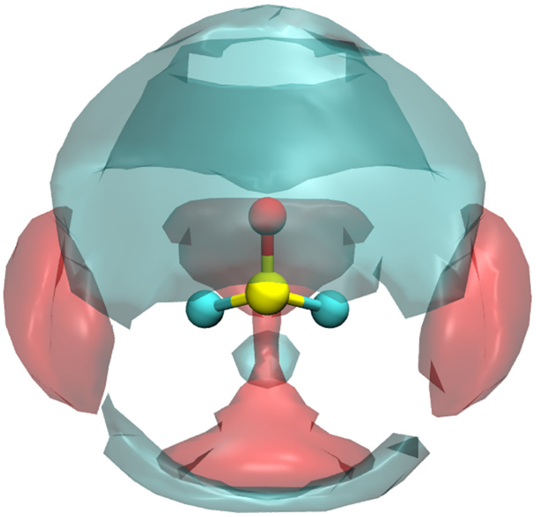

Fig. 11. Spatial distribution function around the reference DMSO molecule in liquid DMSO of O atoms (red surface) and C atoms (cyan surface) of other molecules. The reference frame is defined by the central molecule (hydrogen atoms not shown) and the surfaces represent $g(\boldsymbol{r}) = \boldsymbol{2.5}$. (For interpretation of the references to colour in this figure legend, the reader is referred to the web version of this article.)

nent positive domain located above the reference molecule seems to be related to the locally increased C atoms density. Thus, the significant degree of C—H···O hydrogen bonding in liquid DMSO is largely responsible for increased IR absorption of the discussed fundamental bands. It is worth noting that the positive domains in the spatially resolved IR spectrum of the $\nu^{a}_{\mathrm{C-H}}$ band follow the same pattern, further strengthening the hydrogen bonding interpretation (cf. Fig. S8).

The CH_3 bending modes that displayed their unique character in 2D-COS analysis as discussed above are characterized by a very different picture of spatial correlations. As seen in Fig. 10, both the $\delta^{a}_{\mathrm{CH_3}}$ and the $\delta^{s}_{\mathrm{CH_3}}$ bands show specific spatial patterns that escape trivial comparison with spatial atomic density. In the case of the umbrella mode, although the negative feature "above" the reference molecule, as well as the positive one below, are strictly correlated with increased O atoms density, the two positive domains to the sides are unrelated to any signal detected in SDFs. On the other hand, the unique spatial pattern of the $\delta^{a}_{\mathrm{CH_3}}$ band cannot be compared to any of the examined atomic densities. Consequently, the local dipolar correlations when observed with high spatial resolution go beyond the local correlations in atomic density and rather reflect the dipolar response modulation at specific frequencies by the solvation environment. It is worth noting that the symmetric and antisymmetric components of the $\delta^{a}_{\mathrm{CH_3}}$ band are characterized by qualitatively the same spatial response (see Fig. S8), however, in the case of the antisymmetric mode that manifests in the distance-dependent spectra as a slowly vanishing shoulder the negative correlations are much more pronounced than for the symmetric one.

Finally, the THz mode at ~100 cm^{-1} that in the liquid phase reveals the "mesoscopic" nature of correlated molecular motion [106] is surprisingly only somewhat related to the SDF of CoMs of neighboring molecules. This can mean that only a subset of the first solvation shell DMSO molecules contributes meaningfully to the observed absorption increase of this "cage" mode when going from the intramolecular to the bulk limit. Unlike in liquid water, where hydrogen bonding is ultimately responsible for shaping the spatial correlations in the longitudinal acoustic mode [51], the C—H···O hydrogen bonding in DMSO is much weaker, but still able to imprint the spatial response of the "cage" mode as the shape of the spatial pattern seems to reflect the position of weakly hydrogen bonded DMSO molecules.

Conclusions

DMSO, a very important water-miscible solvent, is characterized by a considerable degree of intermolecular interactions as revealed by lengthy AIMD simulations. Both the structure and dynamics of liquid DMSO are faithfully represented by the applied computational approach as emphasized by detailed comparison to the relevant experimental data. Most importantly, DMSO shows a non-negligible intermolecular term in the IR spectrum of the liquid phase. While the transition from the intramolecular to the bulk limit seems to be predominantly a spectral intensity increase, the fine details of this process can be observed using the novel spectral decomposition techniques. Distance-dependent spectra that allow the detailed observation of spectral intensity unfolding with increasing correlation radius are an invaluable tool for this purpose. Here, the interpretative power of these spectra is effectively strengthened by harnessing the possibilities offered by generalized two-dimensional correlation spectroscopy. Most importantly, we demonstrate unequivocally that specific weak vibrational modes—notably CH_3 bending ones—observable in the intramolecular limit are suppressed by the solvation environment of a DMSO molecule and thus escape detection in the bulk phase IR spectra. This remains in stark contrast to the previously studied liquids, notably H_2O, where the appearance of new vibrational bands accompanied the transition from the intra- to the intermolecular limit. Furthermore, the spatially resolved IR spectra of liquid DMSO reveal the non-trivial character of positive correlations and negative anti-correlations of molecular dipoles that is only indirectly related to the correlations in atomic densities as captured by the relevant SDFs. Certainly, the extent of these correlations goes beyond the dimerization approximation that was previously frequently used to interpret the IR spectrum of liquid DMSO. To sum up, due care must be taken when interpreting IR spectra of even weakly associated molecular liquids, as the intermolecular correlations can shape the measured spectra in a non-negligible and non-trivial manner.

Declaration of Competing Interest

The authors declare that they have no known competing financial interests or personal relationships that could have appeared to influence the work reported in this paper.

Acknowledgments

This work was supported by the statutory fund of Gdańsk University of Technology. Calculations were performed at the Academic Computer Center in Gdańsk (TASK).

Appendix A. Supplementary material

Supplementary data associated with this article can be found, in the online version, at https://doi.org/10.1016/j.saa.2021.119869.

References

[1] E. Buncel, R.A. Stairs, Solvent Effects in Chemistry, Second Edition., John Wiley & Sons Inc, Hoboken, New Jersey, 2016.

[2] D. Martin, H.G. Hauthal, Dimethyl sulphoxide, John Wiley & Sons, New York, 1975.

[3] D. Martin, A. Weise, H.-J. Niclas, The Solvent Dimethyl Sulfoxide, Angew. Chem. Int. Ed. Engl. 6 (1967) 318–334.

[4] W.W. Epstein, F.W. Sweat, Dimethyl Sulfoxide Oxidations, Chem. Rev. 67 (1967) 247–260.

[5] J. Kiefer, K. Noack, B. Kirchner, Hydrogen Bonding in Mixtures of Dimethyl Sulfoxide and Cosolvents, Curr. Phys. Chem. 1 (2011) 340–351.

[6] A.C. Williams, B.W. Barry, Penetration enhancers, Adv. Drug Deliv. Rev. 56 (2004) 603–618.

[7] Z.-W. Yu, P.J. Quinn, Dimethyl sulphoxide: A review of its applications in cell biology, Biosci. Rep. 14 (1994) 259–281.

[8] H. Dreizler, G. Dendl, Rotationsspektrum, r_0-Struktur und Dipolmoment von Dimethylsulfoxyd, Z. Naturforsch. 19a (1964) 512–514.

[9] U. Kaatze, R. Pottel, M. Schäfer, Dielectric Spectrum of Dimethyl Sulfoxide/Water Mixtures as a Function of Composition, J. Phys. Chem. 93 (1989) 5623–5627.

[10] J. Krakowiak, M. Śmiechowski, Excess molar volume and viscosity deviation for binary mixtures of γ-butyrolactone with dimethyl sulfoxide, J. Chem. Thermodyn. 110 (2017) 57–64.

[11] T.B. Douglas, Heats of Formation of Liquid Methyl Sulfoxide and Crystalline Methyl Sulfone at 18, J. Am. Chem. Soc. 68 (1946) 1072–1076.

[12] L.S. Manjeshwar, T.M. Aminabhavi, Densities and Viscosities of Binary Liquid Mixtures Containing Bromoform at 45 C, J. Chem. Eng. Data 33 (1988) 184–185.

[13] B. Long, Experimental Studies and Thermodynamic Modeling of the Solubilities of Potassium Nitrate, Potassium Chloride, Potassium Bromide, and Sodium Chloride in Dimethyl Sulfoxide, Ind. Eng. Chem. Res. 50 (2011) 7019–7026.

[14] S.E. McLain, A.K. Soper, A. Luzar, Orientational correlations in liquid acetone and dimethyl sulfoxide: A comparative study, J. Chem. Phys. 124 (2006) 074502.

[15] U. Onthong, T. Megyes, I. Bakó, T. Radnai, T. Grósz, K. Hermansson, M. Probst, X-ray and neutron diffraction studies and molecular dynamics simulations of liquid DMSO, Phys. Chem. Chem. Phys. 6 (2004) 2136–2144.

[16] A. Luzar, A.K. Soper, D. Chandler, Combined neutron diffraction and computer simulation study of liquid dimethyl sulphoxide, J. Chem. Phys. 99 (1993) 6836–6847.

[17] S. Itoh, H. Ohtaki, A Study of the Liquid Structure of Dimethyl Sulfoxide by the X-Ray Diffraction, Z. Naturforsch. 42a (1987) 858–862.

[18] K.-I. Oh, K. Rajesh, J.F. Stanton, C.R. Baiz, Quantifying Hydrogen-Bond Populations in Dimethyl Sulfoxide/Water Mixtures, Angew. Chem. Int. Ed. 56 (2017) 11375–11379.

[19] G. Upadhyay, T.G. Devi, Raman bandshape analysis on C-H and CSC stretching modes of dimethyl sulfoxide in liquid binary mixture: Comparative study with quantum-chemical calculations, Spectrochim. Acta A 133 (2014) 250–258.

[20] T. Clark, J.S. Murray, P. Lane, P. Politzer, Why are dimethyl sulfoxide and dimethyl sulfone such good solvents?, J Mol. Model. 14 (2008) 689–697.

[21] S.J. Bachmann, W.F. van Gunsteren, Polarizable Model for DMSO and DMSO–Water Mixtures, J. Phys. Chem. B 118 (2014) 10175–10186.

[22] Q. Zhang, X. Zhang, D.-X. Zhao, Polarizable force field for water-dimethyl sulfoxide systems: II properties of mixtures by molecular dynamics simulations, J. Mol. Liquids 145 (2009) 67–81.

[23] M. Chalaris, S. Marinakis, D. Dellis, Temperature effects on the structure and dynamics of liquid dimethyl sulfoxide: A molecular dynamics study, Fluid Phase Equilib. 267 (2008) 47–60.

[24] D.P. Geerke, C. Oostenbrink, N.F.A. van der Vegt, W.F. van Gunsteren, An Effective Force Field for Molecular Dynamics Simulations of Dimethyl Sulfoxide and Dimethyl Sulfoxide-Water Mixtures, J. Phys. Chem. B 108 (2004) 1436–1445.

[25] P. Bordat, J. Sacristan, D. Reith, S. Girard, A. Glättli, F. Müller-Plathe, An improved dimethyl sulfoxide force field for molecular dynamics simulations, Chem. Phys. Lett. 374 (2003) 201–205.

[26] S.M. Vechi, M.S. Skaf, Collision-Induced Effects on the Dielectric Properties of Liquid Dimethylsulfoxide, J. Braz. Chem. Soc. 13 (2002) 583–591.

[27] M.L. Strader, S.E. Feller, A Flexible All-Atom Model of Dimethyl Sulfoxide for Molecular Dynamics Simulations, J. Phys. Chem. A 106 (2002) 1074–1080.

[28] A. Vishnyakov, A.P. Lyubartsev, A. Laaksonen, Molecular Dynamics Simulations of Dimethyl Sulfoxide and Dimethyl Sulfoxide-Water Mixture, J. Phys. Chem. A 105 (2001) 1702–1710.

[29] A.K. Adya, O.N. Kalugin, M.N. Volobuev, Y.V. Kolesnik, Microscopic structure of liquid dimethyl sulphoxide and its electrolyte solutions: molecular dynamics simulations, Mol. Phys. 99 (2001) 835–854.

[30] M.S. Skaf, Molecular dynamics simulations of dielectric properties of dimethyl sulfoxide: Comparison between available potentials, J. Chem. Phys. 107 (1997) 7996–8003.

[31] J.M.M. Cordeiro, Structure of acetone and dimethyl sulfoxide from Monte Carlo simulations and MM2 calculations, Phys. Chem. Liquids 45 (2007) 31–39.

[32] S. Bratos, R.M. Pick (Eds.), Vibrational Spectroscopy of Molecular Liquids and Solids, NATO ASI Series B: Physics, Vol. 56, Springer, US, New York, 1980.

[33] M.Y. Skripkin, P. Lindqvist-Reis, A. Abbasi, J. Mink, I. Persson, M. Sandström, Vibrational spectroscopic force field studies of dimethyl sulfoxide and hexakis(dimethyl sulfoxide)scandium(III) iodide, and crystal and solution structure of the hexakis(dimethyl sulfoxide)scandium(III) ion, Dalton Trans. (2004) 4038–4049.

[34] S. Bayari, Z. Kantarci, S. Akyüz, An infrared spectroscopic study on Hofmann-type complexes of dimethyl sulfoxide, J. Mol. Struct. 351 (1995) 19–24.

[35] M.-T. Forel, M. Tranquille, Spectres de vibration du diméthylsulfoxyde et du diméthylsulfoxyde-d_6, Spectrochim. Acta A 26 (1970) 1023–1034.

[36] V.M. Wallace, N.R. Dhumal, F.M. Zehentbauer, H.J. Kim, J. Kiefer, Revisiting the Aqueous Solutions of Dimethyl Sulfoxide by Spectroscopy in the Mid- and Near-Infrared: Experiments and Car-Parrinello Simulations, J. Phys. Chem. B 119 (2015) 14780–14789.

[37] D. Warmińska, J. Stangret, Application of the tetraphenylphosphonium tetraphenylborate (TPTB) assumption to the thermodynamic properties of solvated ions in dimethylsulfoxide, Phys. Chem. Chem. Phys. 14 (2012) 3176–3180.

[38] W.R. Fawcett, A.A. Kloss, Attenuated total reflection fourier-transform IR spectroscopic study of dimethyl sulfoxide self-association in acetonitrile solutions, J. Chem. Soc., Faraday Trans. 92 (1996) 3333–3337.

[39] W.R. Fawcett, A.A. Kloss, Solvent-Induced Frequency Shifts in the Infrared Spectrum of Dimethyl Sulfoxide in Organic Solvents, J. Phys. Chem. 100 (1996) 2019–2024.

[40] S.A. Kirillov, M.I. Gorobets, M.M. Gafurov, K.S. Rabadanov, M.B. Ataev, Temperature Dependence of Associative Equilibria of DMSO According to Raman Scattering Spectra, Rus. J. Phys. Chem. A 88 (2014) 175–177.

[41] S.A. Kirillov, M.I. Gorobets, M.M. Gafurov, M.B. Ataev, K.S. Rabadanov, Self-Association and Picosecond Dynamics in Liquid Dimethyl Sulfoxide, J. Phys. Chem. B 117 (2013) 9439–9448.

[42] G. Upadhyay, T.G. Devi, R.K. Singh, A. Singh, P.R. Alapati, Solvent dependent frequency shift and Raman noncoincidence effect of S=O stretching mode of dimethyl sulfoxide in liquid binary mixtures, Spectrochim. Acta A 109 (2013) 239–246.

[43] I.S. Perelygin, Band shape in vibrational spectra and interactions of polar molecules in liquids, J. Struct. Chem. 38 (1997) 218–226.

[44] F. Cansell, D. Fabre, J.P. Petitet, Raman spectroscopy of DMSO and DMSO–H2O mixtures (32 mol% of DMSO) up to 20 GPa, Phys. B 182 (1992) 195–200.

[45] J. Świergiel, I. Płowaś, J. Jadżyn, On investigation of aggregation of molecular dipoles in liquids, J. Mol. Liquids 220 (2016) 879–882.

[46] J. Jadżyn, J. Świergiel, On Intermolecular Dipolar Coupling in Two Strongly Polar Liquids: Dimethyl Sulfoxide and Acetonitrile, J. Phys. Chem. B 115 (2011) 6623–6628.

[47] T. Shikata, N. Sugimoto, Reconsideration of the anomalous dielectric behavior of dimethylsulfoxide in the pure liquid state, Phys. Chem. Chem. Phys. 13 (2011) 16542–16547.

[48] G. Ritzoulis, Excess properties of the binary liquid systems dimethylsulfoxide + isopropanol and propylene carbonate + isopropanol, Can. J. Chem. 67 (1989) 1105–1108.

[49] E.W. Prestbo, J.L. McHale, Static Dielectric Constants and Kirkwood Correlation Factors of Dimethyl Sulfoxide/Carbon Tetrachloride Solutions, J. Chem. Eng. Data 29 (1984) 387–389.

[50] R.L. Amey, Extent of association in liquid dimethyl sulfoxide, J. Phys. Chem. 72 (1968) 3358–3359.

[51] M. Heyden, J. Sun, H. Forbert, G. Mathias, M. Havenith, D. Marx, Understanding the Origins of Dipolar Couplings and Correlated Motion in the Vibrational Spectrum of Water, J. Phys. Chem. Lett. 3 (2012) 2135–2140.

[52] M. Heyden, J. Sun, S. Funkner, G. Mathias, H. Forbert, M. Havenith, D. Marx, Dissecting the THz spectrum of liquid water from first principles via correlations in time and space, Proc. Natl. Acad. Sci. U.S.A. 107 (2010) 12068–12073.

[53] R. Iftimie, M.E. Tuckerman, Decomposing total IR spectra of aqueous systems into solute and solvent contributions: A computational approach using maximally localized Wannier orbitals, J. Chem. Phys. 122 (2005) 214508.

[54] M.-P. Gaigeot, M. Sprik, Ab Initio Molecular Dynamics Computation of the Infrared Spectrum of Aqueous Uracil, J. Phys. Chem. B 107 (2003) 10344–10358.

[55] M. Śmiechowski, Visualizing spatially decomposed intermolecular correlations in the infrared spectra of aprotic liquids, J. Mol. Graph. Model. 78 (2017) 148–157.

[56] M. Śmiechowski, J. Krakowiak, P. Bruździak, J. Stangret, Unique Agreement of Experimental and Computational Infrared Spectroscopy: a Case Study of Lithium Bromide Solvation in an Important Electrochemical Solvent, Phys. Chem. Chem. Phys. 19 (2017) 9270–9280.

[57] D. Marx, J. Hutter, Ab Initio Molecular Dynamics, Cambridge University Press, Cambridge, 2009.

[58] A.A. Hassanali, J. Cuny, V. Verdolino, M. Parrinello, Aqueous solutions: state of the art in ab initio molecular dynamics, Philos. Trans. R. Soc. A 372 (2014) 20120482.

[59] A. Korotkevich, D.S. Firaha, A.A.H. Padua, B. Kirchner, Ab initio molecular dynamics simulations of SO_2 solvation in choline chloride/glycerol deep eutectic solvent, Fluid Phase Equil. 448 (2017) 59–68.

[60] M. Callsen, K. Sodeyama, Z. Futera, Y. Tateyama, I. Hamada, The Solvation Structure of Lithium Ions in an Ether Based Electrolyte Solution from First-Principles Molecular Dynamics, J. Phys. Chem. B 121 (2017) 180–188.

[61] K.H. Wujcik, T.A. Pascal, C.D. Pemmaraju, D. Devaux, W.C. Stolte, N.P. Balsara, D. Prendergast, Characterization of Polysulfide Radicals Present in an Ether-Based Electrolyte of a Lithium-Sulfur Battery During Initial Discharge Using In Situ X-Ray Absorption Spectroscopy Experiments and First-Principles Calculations, Adv. Energy Mater. 5 (2015) 1500285.

[62] M. Pu, T. Privalov, Ab Initio Molecular Dynamics with Explicit Solvent Reveals a Two-Step Pathway in the Frustrated Lewis Pair Reaction, Chem. Eur. J. 21 (2015) 17708–17720.

[63] A. Panuszko, P. Bruździak, M. Śmiechowski, M. Stasiulewicz, J. Stefaniak, J. Stangret, DMSO hydration redefined: Unraveling the hydrophobic hydration of solutes with a mixed hydrophilic–hydrophobic characteristic, J. Mol. Liquids 294 (2019) 111661.

[64] B. Kirchner, J. Hutter, Solvent effects on electronic properties from Wannier functions in a dimethyl sulfoxide/water mixture, J. Chem. Phys. 121 (2004) 5133–5142.

[65] B. Kirchner, J. Hutter, The structure of a DMSO–water mixture from Car-Parrinello simulations, Chem. Phys. Lett. 364 (2002) 497–502.

[66] I. Noda, Y. Ozaki, Two-dimensional Correlation Spectroscopy – Applications in Vibrational and Optical Spectroscopy, John Wiley & Sons Ltd, Chichester, UK, 2004.

[67] D.A. McQuarrie, Statistical Mechanics, Harper & Row, New York, 1976.

[68] R. Ramírez, T. López-Ciudad, P. Kumar, D. Marx, Quantum corrections to classical time-correlation functions: Hydrogen bonding and anharmonic floppy modes, J. Chem. Phys. 121 (2004) 3973–3983.

[69] M. Thomas, M. Brehm, R. Fligg, P. Vöhringer, B. Kirchner, Computing vibrational spectra from ab initio molecular dynamics, Phys. Chem. Chem. Phys. 15 (2013) 6608–6622.

[70] P.L. Silvestrelli, N. Marzari, D. Vanderbilt, M. Parrinello, Maximally-Localized Wannier Functions For Disordered Systems: Application To Amorphous Silicon, Solid State Commun. 107 (1998) 7–11.

[71] P.L. Silvestrelli, M. Parrinello, Structural, electronic, and bonding properties of liquid water from first principles, J. Chem. Phys. 111 (1999) 3572–3580.

[72] M. Thomas, M. Brehm, B. Kirchner, Voronoi dipole moments for the simulation of bulk phase vibrational spectra, Phys. Chem. Chem. Phys. 17 (2015) 3207–3213.

[73] S. Morita, Y. Ozaki, Moving-window two-dimensional correlation spectroscopy and perturbation-correlation moving-window two-dimensional correlation spectroscopy, Chemom. Intell. Lab. Syst. 168 (2017) 114–120.

[74] M. Thomas, H.H. Richardson, Two-dimensional FT-IR correlation analysis of the phase transitions in a liquid crystal, 4’-n-octyl-4-cyanobiphenyl (8CB), Vib. Spectrosc. 24 (2000) 137–146.

[75] S. Morita, H. Shinzawa, R. Tsenkova, I. Noda, Y. Ozaki, Computational simulations and a practical application of moving-window two-dimensional correlation spectroscopy, J. Mol. Struct. 799 (2006) 111–120.

[76] D.L. Bergman, L. Laaksonen, A. Laaksonen, Visualization of solvation structures in liquid mixtures, J. Mol. Graph. Model. 15 (1997) 301–306.

[77] D. Yokogawa, H. Sato, S. Sakaki, New evaluation of reconstructed spatial distribution function from radial distribution functions, J. Chem. Phys. 125 (2006) 114102.

[78] I.M. Svishchev, P.G. Kusalik, Structure in liquid methanol from spatial distribution functions, J. Chem. Phys. 100 (1994) 5165–5171.

[79] F. Neese, The ORCA program system, WIREs Comput. Mol. Sci. 2 (2012) 73–78.

[80] A.D. Becke, Density-functional exchange-energy approximation with correct asymptotic behavior, Phys. Rev. A 38 (1988) 3098–3100.

[81] C. Lee, W. Yang, R.G. Parr, Development of the Colle-Salvetti correlation-energy formula into a functional of the electron density, Phys. Rev. B 37 (1988) 785–789.

[82] S. Grimme, J. Antony, S. Ehrlich, H. Krieg, A consistent and accurate ab initio parametrization of density functional dispersion correction (DFT-D) for the 94 elements H-Pu, J. Chem. Phys. 132 (2010) 154104.

[83] F. Weigend, R. Ahlrichs, Balanced basis sets of split valence, triple zeta valence and quadruple zeta valence quality for H to Rn: Design and assessment of accuracy, Phys. Chem. Chem. Phys. 7 (2005) 3297–3305.

[84] A. Schaefer, H. Horn, R. Ahlrichs, Fully optimized contracted Gaussian basis sets for atoms Li to Kr, J. Chem. Phys. 97 (1992) 2571–2577.

[85] J. VandeVondele, M. Krack, F. Mohamed, M. Parrinello, T. Chassaing, J. Hutter, Quickstep: Fast and accurate density functional calculations using a mixed Gaussian and plane waves approach, Comp. Phys. Commun. 167 (2005) 103–128.

[86] The cp2k Developers Group, cp2k v. 2.7, http://www.cp2k.org/ (2001–2015).

[87] J. Hutter, M. Iannuzzi, F. Schiffmann, J. VandeVondele, cp2k: atomistic simulations of condensed matter systems, WIREs Comput. Mol. Sci. 4 (2014) 15–25.

[88] G. Lippert, J. Hutter, M. Parrinello, A hybrid Gaussian and plane wave density functional scheme, Mol. Phys. 92 (1997) 477–487.

[89] S. Goedecker, M. Teter, J. Hutter, Separable dual-space Gaussian pseudopotentials, Phys. Rev. B 54 (1996) 1703–1710.

[90] L. Martínez, R. Andrade, E.G. Birgin, J.M. Martínez, Packmol: A package for building initial configurations for molecular dynamics simulations, J. Comput. Chem. 30 (2009) 2157–2164.

[91] G.J. Martyna, M.L. Klein, M. Tuckerman, Nosé-Hoover chains: The canonical ensemble via continuous dynamics, J. Chem. Phys. 97 (1992) 2635–2643.

[92] J. VandeVondele, F. Mohamed, M. Krack, J. Hutter, M. Sprik, M. Parrinello, The influence of temperature and density functional models in ab initio molecular dynamics simulation of liquid water, J. Chem. Phys. 122 (2005) 014515.

[93] E. Schwegler, J.C. Grossman, F. Gygi, G. Galli, Towards an assessment of the accuracy of density functional theory for first principles simulations of water. II, J. Chem. Phys. 121 (2004) 5400–5409.

[94] M. Śmiechowski, J. Sun, H. Forbert, D. Marx, Solvation shell resolved THz spectra of simple aqua ions – distinct distance- and frequency-dependent contributions of solvation shells, Phys. Chem. Chem. Phys. 17 (2015) 8323–8329.

[95] S.A. Markarian, A.M. Terzyan, Surface Tension and Refractive Index of Dialkylsulfoxide + Water Mixtures at Several Temperatures, J. Chem. Eng. Data 52 (2007) 1704–1709.

[96] M. Tuckerman, Statistical Mechanics: Theory and Molecular Simulation, Oxford University Press, New York, 2010.

[97] M. Wojdyr, Fityk: a general-purpose peak fitting program, J. Appl. Cryst. 43 (2010) 1126–1128.

[98] W. Humphrey, A. Dalke, K. Schulten, VMD: Visual Molecular Dynamics, J. Mol. Graph. 14 (1996) 33–38.
[99] R. Kumar, J.R. Schmidt, J.L. Skinner, Hydrogen bonding definitions and dynamics in liquid water, J. Chem. Phys. 126 (2007) 204107.
[100] A. Luzar, Resolving the hydrogen bond dynamics conundrum, J. Chem. Phys. 113 (2000) 10663–10675.
[101] M.J. McGrath, I.-F.W. Kuo, J.I. Siepmann, Liquid structures of water, methanol, and hydrogen fluoride at ambient conditions from first principles molecular dynamics simulations with a dispersion corrected density functional, Phys. Chem. Chem. Phys. 13 (2011) 19943–19950.
[102] M. Holz, S.R. Heil, A. Sacco, Temperature-dependent self-diffusion coefficients of water and six selected molecular liquids for calibration in accurate ^{1}H NMR PFG measurements, Phys. Chem. Chem. Phys. 2 (2000) 4740–4742.
[103] H. Kovacs, J. Kowalewski, A. Maliniak, Sulfur-33 Relaxation and Nuclear Quadrupole Coupling Constant in Dimethylsulfoxide, Acta Chem. Scand. 41a (1987) 471–479.
[104] S. Imoto, P. Kibies, C. Rosin, R. Winter, S.M. Kast, D. Marx, Toward Extreme Biophysics: Deciphering the Infrared Response of Biomolecular Solutions at High Pressures, Angew. Chem. Int. Ed. 55 (2016) 9533–9537.
[105] M.A. Czarnecki, Interpretation of Two-Dimensional Correlation Spectra: Science or Art?, Appl. Spectrosc. 52 (1998) 1583–1590.
[106] D.A. Turton, J. Hunger, A. Stoppa, A. Thoman, M. Candelaresi, G. Hefter, M. Walther, R. Buchner, K. Wynne, Rattling the cage: Micro- to mesoscopic structure in liquids as simple as argon and as complicated as water, J. Mol. Liquids 159 (2011) 2–8.